CHIN. PHYS. LETT. Vol. 36, No. 10 (2019) 100303 **Express Letter**

Experimental Hamiltonian Learning of an 11-Qubit Solid-State Quantum Spin Register *

P.-Y. Hou(侯攀宇)†, L. He(何丽)†, F. Wang(王飞)†, X.-Z. Huang(黄晛之), W.-G. Zhang(张文纲), X.-L. Ouyang(欧阳晓龙), X. Wang(王歆), W.-Q. Lian(连文倩), X.-Y. Chang(常秀英), L.-M. Duan(段路明)**

Center for Quantum Information, Institute for Interdisciplinary Information Sciences, Tsinghua University, Beijing 100084

(Received 23 September 2019)

Learning the Hamiltonian of a quantum system is indispensable for prediction of the system dynamics and realization of high fidelity quantum gates. However, it is a significant challenge to efficiently characterize the Hamiltonian which has a Hilbert space dimension exponentially growing with the system size. Here, we develop and implement an adaptive method to learn the effective Hamiltonian of an 11-qubit quantum system consisting of one electron spin and ten nuclear spins associated with a single nitrogen-vacancy center in a diamond. We validate the estimated Hamiltonian by designing universal quantum gates based on the learnt Hamiltonian and implementing these gates in the experiment. Our experimental result demonstrates a well-characterized 11-qubit quantum spin register with the ability to test quantum algorithms, and shows our Hamiltonian learning method as a useful tool for characterizing the Hamiltonian of the nodes in a quantum network with solid-state spin qubits.

PACS: 03.67.−a DOI: 10.1088/0256-307X/36/10/100303

Experimental realization of quantum registers is an essential task in quantum information processing (QIP). Lots of efforts towards this goal have been made on various systems such as trapped ions,[1−3] solid-state spins,[4−14] neutral atoms[15] and superconducting qubits.[16−19] One important system is the solid-state spin system associated with a single nitrogen vacancy (NV) center in a bulk diamond, which has been demonstrated to be a promising platform for quantum network,[4−9] quantum computing,[12,20] and quantum sensing.[21−26] This system consists of one electron spin and multiple surrounding nuclear spins which are mostly provided by ^{13}C atoms in the diamond lattice. It has been demonstrated that the electron spin could be initialized and detected by optical method, and manipulated with high fidelity by microwave signals.[27,28] It is difficult to detect the surrounding nuclear spins directly, however, the dynamical decoupling (DD) technique has been well developed for universal control of nuclear spins,[4,10−12,29−32] which is essentially realized by manipulating the electron spin with a DD sequence. Moreover, initialization and detection of nuclear spins can be implemented by a set of the DD-type gates.[4,12,20] The electron spins of two remote NV centers can be entangled through photonic links,[8,33,34] which leads to a promising path to a scalable quantum network based solid-state spin quantum register associated with NV centers in diamond.

In this solid-state spin register, it is worthwhile to precisely characterize system Hamiltonian by learning the interaction parameters because: (1) the parameters of the DD-type nuclear spin gate are determined by the hyperfine interaction between the electron spin and the target nuclear spin, (2) the interactions among all the spin qubits are constantly on, so that it is inevitable to have crosstalk errors from the other nuclear spins while controlling the target nuclear spin. With the Hamiltonian parameters, dynamical decoupling sequence could be optimized to realize the desired operation on the target nuclear spin, in the mean time to reduce the gate errors due to unwanted crosstalk. In this work, we experimentally characterize the effective Hamiltonian of an NV center system composed of one electron spin and ten weakly coupled ^{13}C nuclear spins. We first perform the DD spectroscopy to probe the surrounding spin environment which is realized by applying a DD sequence on the electron spin with a varying interpulse time. From the resulting DD spectrum, we identify 10 dominant nuclear spins which give strong signals to the electron spin coherence. We ignore the nuclear-nuclear interaction in this 11-qubit system because their strength is at least 1 order lower compared to electron-nuclear spin-spin interaction. Therefore, the essential Hamiltonian parameters are the parameters of the hyperfine interactions between the NV electron spin and each of the resolved 10 nuclear spins. We first roughly extract these hyperfine interaction parameters by fitting the simulated data to the experimental DD spectrum.

*Supported by the Frontier Science Center for Quantum Information of the Ministry of Education of China, Tsinghua University Initiative Scientific Research Program, and the National Key Research and Development Program of China (2016YFA0301902).

†They contributed equally to this work.

**Corresponding author. Email: lmduan@tsinghua.edu.cn

© 2019 Chinese Physical Society and IOP Publishing Ltd

Then, we precisely learn the hyperfine parameters of each nuclear spin by measuring the nuclear Larmor frequencies with different electron spin states. We apply an adaptive method[35,36] based on the quantum phase estimation algorithm in a sequence of Ramsey-interferometry experiments to improve the efficiency of the frequency measurements. To validate the estimated Hamiltonian parameters, we numerically optimized quantum gates based on the learnt Hamiltonian parameters and experimentally implemented a universal set of quantum gates for this 11-qubit system.

We performed the experiments at a cryogenic temperature (∼8 K) on a type-IIa CVD synthetic diamond sample with the natural abundance of ^{13}C (∼1.1%). The 11-qubit system was composed of 1 NV electron spin $S = 1$ ($|m_s = 0\rangle \equiv |0\rangle, |m_s = \pm 1\rangle \equiv |\pm 1\rangle$) and 10 ^{13}C nuclear spins $I = 1/2$ ($|m_I = \frac{1}{2}\rangle \equiv |\uparrow\rangle, |m_I = -\frac{1}{2}\rangle \equiv |\downarrow\rangle$). The NV electron spin can be optically initialized with a fidelity over 99% through the intersystem crossing[13] and read out in a single shot with an average fidelity of 90% ($F_0 = 81\%$ for $|0\rangle$ state and $F_1 = 99\%$ for $|\pm 1\rangle$ states) in Fig. 1(b). With a magnetic field B_z (∼495 gauss) along the NV symmetry axis, the Hamiltonian of the 11-qubit system is described by

$$\hat{\boldsymbol{H}} = D \cdot \hat{S}_z^2 + \gamma_e B_z \hat{S}_z + \sum_i (\hat{\boldsymbol{S}} \cdot \hat{\boldsymbol{A}}_i \cdot \hat{\boldsymbol{I}}_i + \gamma_n B_z \hat{I}_{i,z}), \tag{1}$$

where the NV symmetry axis is defined as the z axis. The electron (nuclear) spin operator $\hat{\boldsymbol{S}}$ ($\hat{\boldsymbol{I}}$) contains the Pauli matrices $\hat{S}_x$, $\hat{S}_y$, $\hat{S}_z$ ($\hat{I}_x$, $\hat{I}_y$, $\hat{I}_z$); D is the zero-field splitting of 2.8776 GHz; γ_e (γ_n) is the gyromagnetic ratio of the electron spin (^{13}C nuclear spin); $\hat{\boldsymbol{A}}_i$ is the tensor of hyperfine interaction between the electron spin and the nuclear spin i. Dipole-dipole interactions between nuclear spins are typically negligible.

In the rotating frame defined by the Hamiltonian $H_0 = D\hat{S}_z^2 + \gamma_e B_z \hat{S}_z$, by neglecting the fast oscillation terms, we derive the effective Hamiltonian, which is described by

$$\hat{\boldsymbol{H}}_{\text{eff}} = \sum_i (A_{i,zx}\hat{S}_z\hat{I}_{i,x} + A_{i,zy}\hat{S}_z\hat{I}_{i,y} + A_{i,zz}\hat{S}_z\hat{I}_{i,z} + \gamma_n B_z \hat{I}_{i,z}) = \sum_i \hat{H}_i. \tag{2}$$

In Eq. (2), the effective Hamiltonian $\hat{\boldsymbol{H}}_{\text{eff}}$ equals the sum of the subsystem Hamiltonians $\hat{H}_i$, which describes the hyperfine interaction between the electron spin and nuclear spin i. In particular, $\hat{H}_i$ can be simplified to $\hat{H}_i^{'} = A_{i,zx}^{'}\hat{S}_z\hat{I}_{i,x} + A_{i,zz}^{'}\hat{S}_z\hat{I}_{i,z} + \gamma_n B_z \hat{I}_{i,z}$ by redefining the x axis for each nuclear spin so that $A_{zy}^{'} = 0$ (the x, y axes for different nuclear spins can be defined independently as we have ignored the direct coupling terms between the nuclear spins). In the following, to simplify notation, we denote $A_{zz}^{'}$ and $A_{zx}^{'}$ in the rotated frame still as A_{zz} and A_{zx} by setting $A_{zy}^{'} = 0$. Therefore, the main task of learning the whole system Hamiltonian is simplified as characterization of the hyperfine parameters $\{A_{zz}, A_{zx}\}$ for all the nuclear spins.

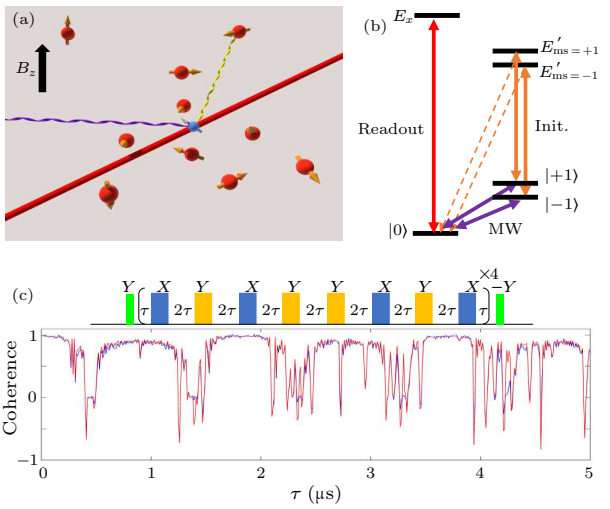

Fig. 1. (a) Illustration of an NV center system consisting of one electron spin (blue ball) and multiple nuclear spins (red balls). The electron spin is optically initialized and read out by the resonant laser (red line), manipulated by microwave fields (purple wave). (b) Diagram of relevant energy levels of the NV center, where $|0\rangle$ ($|\pm 1\rangle$) denotes respectively the bright (dark) state under a readout laser, and they are coherently manipulated by microwave signals. The state $|\pm 1\rangle$ can be optically pumped to $|0\rangle$ by an initialization laser. (c) Dynamical decoupling spectrum probed by the electron spin with a CPMG-32 pulse sequence. Blue and red lines denote the experimental data and the simulation results for the 10 resolved nuclear spins, respectively.

To explore the spin environment of an NV center, we prepared the electron spin in a superposition $(|0\rangle + |-1\rangle)/\sqrt{2}$ with a $\pi/2$ pulse after optical initialization and applied a Carr–Purcell–Meiboom–Gill (CPMG) type of DD sequence with 32 π-pulses. The CPMG sequence was formed by $N = 32$ π-pulses with the configuration of $(\tau - \pi - \tau)^{\times N}$, where 2τ was the interval between two neighboring π-pulses. The phase of π-pulses in the CPMG sequence followed the XY-8 scheme shown in Fig. 1(c). The electron spin coherence was read out by projecting the final state on the x basis with a second $\pi/2$ pulse. By scanning pulse interval τ in the range of $0 < \tau < 50\,\mu$s, we obtained the DD spectrum which was the electron spin coherence as a function of τ. Ten nuclear spins that gave strong coherence decay signals were resolved from the spectrum using the method in Ref. [11] By fitting the simulation results to the experimental DD spectrum, the hyperfine parameters $\{A_{zz}, A_{zx}\}$ of 10 resolved nuclear spins were extracted with limited precision. This precision was limited because all the nuclear spins, in-

cluding the unresolved ones, contributed collectively to the DD spectrum, which made it hard to estimate the hyperfine parameters of each nuclear spin individually. However, these extracted hyperfine parameters, although with limited precision, still allowed us to perform quantum gates on the electron and nuclear spins with relatively low fidelities. With these gates, the 10 nuclear spins could be polarized with the fidelities ranging from 55% to 85%.

Nuclear spin Larmor precession frequency is affected by the hyperfine interaction with the electron spin. For a weakly coupled ^{13}C nuclear spin, $f_{\pm}$, defined as the precession frequency of the nuclear spin when the electron spin is in the $|\pm 1\rangle$ state, is given by

$$f_{\pm} = \frac{1}{2\pi}\sqrt{A_{xz}^2 + (A_{zz} \pm \omega_n)^2}, \tag{3}$$

where $\omega_n = \gamma_n B_z$. To precisely calibrate the parameters $\{A_{zz}, A_{zx}\}$ of each nuclear spin, we roughly polarized the target nuclear spin, and measured its precession frequency with the electron spin at $|+1\rangle$ and $|-1\rangle$ state. In this case, precision of $\{A_{zz}, A_{zx}\}$ was only determined by that of $f_{\pm}$, and was not affected by other nuclear spins, which were at fully mixed states so that they did not contribute to the measured signals.

To improve efficiency in measuring these precession frequencies,[37] we implemented an adaptive quantum phase estimation algorithm. The basic idea of this adaptive scheme is to perform a sequence of Ramsey interferometry experiments with different precession time $t_n = 2^{N-n}t_{\min}(n = 1, \ldots, N)$, so that the frequency probability distribution is updated after each Ramsey experiment and the frequency estimation range is gradually narrowed down. In each Ramsey experiment, the target nuclear spin is prepared into a superposition state $(|\uparrow\rangle + |\downarrow\rangle)/\sqrt{2}$ and the electron spin is prepared in the $|+1\rangle$ or $|-1\rangle$ state for measuring f_+ or f_-. Then, the target nuclear spin state freely evolves to $(|\uparrow\rangle + e^{i\phi_n}|\downarrow\rangle)/\sqrt{2}$ after t_n, where $\phi_n = 2\pi f t_n$ carries the information of the to-be-measured frequency f. Before the projective measurement of the nuclear spin along the x axis, a rotation $\hat{R}_Z^{\vartheta_n}$ along the z axis with an appropriate angle ϑ_n is applied on the nuclear spin to effectively change the measurement basis. Finally, the nuclear spin is measured with a probability $P_n = \frac{1+\cos(\phi_n - \vartheta_n)}{2}$ in $|\uparrow\rangle$.

The essential idea of this method is to use P_n to update the frequency probability distribution by Bayesian inference and adaptively change the measurement basis based on the previous outcomes, i.e., to deduce the best rotation angle ϑ_{n+1} with $\{P_1, \ldots, P_{n-1}\}$ for minimizing the uncertainty of P_{n+1} through the semiclassical implementation of the quantum phase estimation algorithm.[37] After N-step Ramsey experiments, the frequency is estimated to be the value which gives the highest probability. The to-be-measured frequency f can be represented with a binary digit form $f = \sum_{n=1}^{N} 2^n \cdot k_n \cdot f_0 + \varepsilon$ (see details in the Supplementary Material), where k_n equals 0 or 1 determining $P_n > 0.5$ or $P_n < 0.5$, $f_0 = \frac{1}{2t_{\max}}$ is the measured precision with $t_{\max}$ representing the longest precession time of nuclear spin, and $\varepsilon < f_0$ represents the error term.

We performed the Ramsey interferometry experiments sequentially with precession time $t_n = 2^{N-n}t_{\min}(n = 1, \ldots, N)$, so that k_n was updated one by one, starting from the least significant digit. Each Ramsey experiment was repeated 1000 times. The angle of the Z-rotation gate was updated with $\vartheta_{n+1} = \frac{\vartheta_n}{2} + \frac{k_n \pi}{2}$ starting with the initial phase $\vartheta_1 = \frac{\pi}{2}$. In the experiment, we chose $t_{\min} = 800$ ns to make sure ϕ_n within $(0, \pi]$. The maximal time $t_{\max} = 2^{N-1}t_{\min}$ was determined by the nuclear spin coherence time which is typically around 10 ms. Figure 2(c) shows an example of the frequency estimation result. Here k_n (red circles) were estimated to be 0 or 1 determined by $P_n > 0.5$ or $P_n < 0.5$. By adaptively changing the measurement basis, P_n moved away from 0.5 (k_n approaches 0 or 1) in the quantum phase estimation algorithm, but eventually it was limited by the nuclear spin polarization fidelity. For the first Ramsey experiment, P_0 was measured to be near 0.5 because of no adaptive change of the basis before this measurement and a significant decoherence during the long precession time.

Two major imperfections affected the precision in measurement of the precession frequency: (i) nuclear spin decoherence, (ii) magnetic field misalignment. Limited by the first kind of imperfection, we chose $t_{\max}$ to be smaller than nuclear spin coherence time. To suppress the influence of the second kind, we calibrated the transverse magnetic field B_x to be near zero by minimizing the sum of the two electron spin resonant frequencies $f_{|0\rangle \leftrightarrow |\pm 1\rangle}$. However, the intrinsic short coherence time of the electron spin led to a wide resonance linewidth so that B_x could only be calibrated to be smaller than 2.5 gauss. The residual B_x field could cause a fairly large error in the nuclear spin precession frequency, which was estimated by the form

$$\Delta f_+ \approx \frac{(A_{zz} \pm \omega_n)A_{zx}\omega_{ex}}{f_{\pm}(D \pm \omega_e)} \pm \frac{A_{zx}\omega_{nx}}{f_{\pm}}, \tag{4}$$

where $\omega_{ex} = \gamma_e B_x$, $\omega_{nx} = \gamma_n B_x$ (see details in the Supplementary Material).

Hyperfine parameters A_{zz}, A_{zx} of the resolved nuclear spins were calculated by Eq. (3) and (4), and listed in Table 1. With this precisely calibrated hyperfine parameters, we numerically simulated the DD spectrum and compared the simulation results with the experimental data. In Fig. 1(c), the simulation results coincided with most of the signals in the spectrum, and the deviations in certain regions were caused by the unresolved nuclear spin bath.

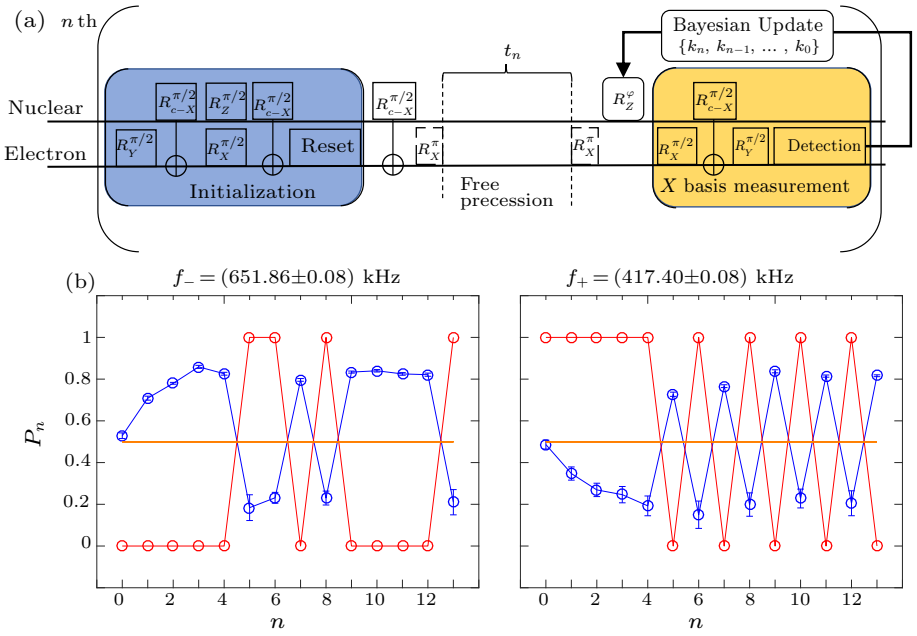

Fig. 2. (a) Experimental sequence to measure the nuclear spin precession frequency under different states of the electron spin through an adaptive method based on the quantum phase estimation algorithm. (b) Frequency measurement results of f_- (left panel) and f_+ (right panel). In the nth Ramsey experiment, k_n (red circle) is estimated by the corresponding outcome of probability P_n (blue circles with the error bar).

Table 1. Measured nuclear spin hyperfine parameters and initialization fidelities. The number in the bracket denotes the error bar in the last digit.

No.	1	2	3	4	5
A_{zx} (kHz)	208(1)	72(1)	72(1)	71(1)	43(1)
A_{zz} (kHz)	566.0(3)	45.9(1)	−15.1(1)	118.1(1)	5.50(7)
F_{init} (%)	95(2)	94(1)	93(1)	97(1)	92(1)
No.	6	7	8	9	10
A_{zx} (kHz)	33(1)	32(1)	31(1)	29(1)	17(1)
A_{zz} (kHz)	−49.64(5)	46.34(5)	27.09(5)	28.70(5)	−14.28(3)
F_{init} (%)	93(1)	81(1)	78(1)	78(1)	86(1)

With the precisely characterized parameters, we designed a universal set of quantum gates for this 11-spin register by simulation, including the single-qubit gates ($\hat{R}_X^{\pi/2}, \hat{R}_Z^{\pi/2}, \hat{R}_Z^{\pi/4}$ with subscript and superscript representing rotation axis and angle respectively) for each electron and nuclear spin, and the controlled rotation gates ($\hat{R}_{c-X}^{\pi/2}$ with electron spin the controlling qubit) between the electron and each nuclear spin. To eliminate crosstalk caused by the constantly-on interactions between electron and other nuclear spins, we numerically optimized the target gate sequence by taking into account the Hamiltonian of other resolved nuclear spins. In addition, to model the unresolved nuclear spins, we randomly chose 10 additional nuclear spins with the interaction parameters uniformly distributed in the range $|A_{zz}, A_{zx}| < 10\,\text{kHz}$ (this range was reasonable as for nuclear spins with larger hyperfine parameters, they should have been identified already) in the simulation. Nuclear spin single-qubit gates were designed by minimizing gate duration to mitigate the decoherence effect. Controlled entangling gates $\hat{R}_{c-X}^{\pi/2}$ were optimized by minimizing the crosstalk to other nuclear spins.

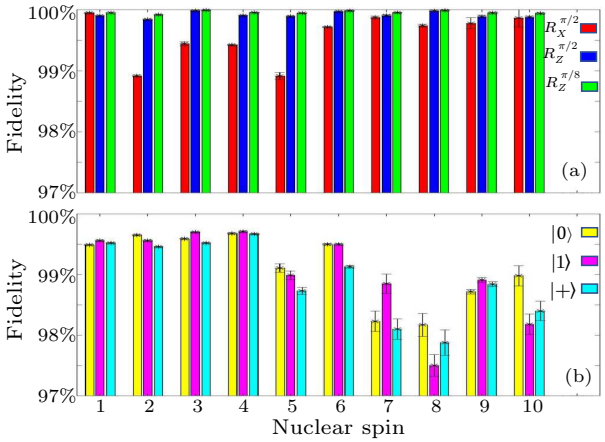

Fig. 3. Histogram of estimated gate fidelities for the 10 resolved nuclear spins. (a) Estimated gate fidelities of single-qubit gates $\hat{R}_X^{\pi/2}, \hat{R}_Z^{\pi/2}, \hat{R}_Z^{\pi/4}$ for each nuclear spin. (b) The fidelities of the entangling gates $\hat{R}_{c-X}^{\pi/2}$ between the electron spin and each nuclear spin under different initial states $|e\uparrow\rangle$, $|e\rangle = |0\rangle, |1\rangle, |+\rangle$ for the control qubit (electron spin). The gate fidelities are estimated through fit to the decay of the state fidelity under repeated application of the same gates.

In the experiment, we used these optimized nuclear spin gate parameters from simulation to polarize the resolved nuclear spins with fidelities shown in Table 1. The fidelities were significantly improved compared with that when we had only a rough estimation of the hyperfine interaction parameters through the DD spectrum. To evaluate the learnt hyperfine parame-

ters, we applied a calibration method[38,39] to estimate the errors of the gates derived from these hyperfine parameters, in which overall state fidelity decays were investigated by repeatedly applying same gates on a certain initial state. By using this method, we could only get the partial information of the gate errors and obtained gate fidelities which were likely higher than the actual gate fidelities, because some unitary errors could be canceled by repeating the gate. However, it gave a rough indicator of the gate fidelity and was sufficient for validating the learnt hyperfine parameters. To analyze single-qubit gate error, we polarized nuclear spins to the $|\uparrow\rangle$ state and applied the same gate M times so that the net operation was an identity, and measured the state fidelity between the outcome state and the ideal target state. The gate fidelity F_{gate} was deduced by fitting the state fidelity decay $F_{\text{state}}(M)$ with a linear function $F_{\text{state}} = F_{\text{init}} - M \cdot F_{\text{gate}}$, where F_{init} was the nuclear spin initialization fidelity. To eliminate the potential bias in the electron initialization state, we repeated the experiments with electron spin in $|0\rangle$ and $|-1\rangle$ state respectively. Final gate fidelities shown in Fig. 3(a) were estimated with the average value of the two cases.

Analogous to single-qubit gate fidelity estimation, we also estimated the fidelity of the two-qubit entangling gate $\hat{R}^{\pi/2}_{c-X}$ by measuring the electron-nuclear spin joint state fidelity. We prepared the electron spin in $|0\rangle, |-1\rangle$ and $|+\rangle = (|0\rangle + |-1\rangle)/\sqrt{2}$ states, respectively, and showed the corresponding results in Fig. 3(b). Each nuclear spin was initialized to the $|\uparrow\rangle$ state. The results indicated that the two-qubit gate $\hat{R}^{\pi/2}_{c-X}$ fidelities of the strongly coupled nuclear spins with strong hyperfine interaction strength were higher than that of weakly coupled nuclear spins. It implied that the spin bath still introduced crosstalk error to the gate operations of the resolved nuclear spins and the weakly coupled nuclear spins suffered more crosstalk to the spin bath than the strongly coupled ones.

In summary, we have experimentally learnt the effective Hamiltonian of an 11-qubit solid-state quantum spin register in a diamond NV center. The learning of the Hamiltonian parameters was implemented by combining the rough parameter estimation from the DD spectrum and the precise determination of each parameter through the adaptive measurement of the nuclear spin precession frequency with the semiclassical quantum phase estimation algorithm. As an example application of the learnt multi-qubit interaction Hamiltonian with precisely determined parameters, we designed and optimized a universal set of quantum gates on these 11 spin qubits under the constantly-on interaction and used the knowledge of the learnt interaction parameters to minimize the crosstalk errors. In future, we could implement longer dynamical decoupling sequences to identify other more weakly coupled nuclear spins from the spin bath. This knowledge would help to further improve the initialization and the gate fidelities for those weakly coupled nuclear spins and reduce the crosstalk error between them. Some of the Hamiltonian learning techniques adopted here, such as the two-step protocol and the adaptive quantum phase estimation algorithm, may also find applications in other multi-qubit systems to characterize the full interaction Hamiltonian and to minimize the crosstalk errors for quantum gate operations.

Note Added: After completion of this work, we became aware of a related work[40] that demonstrated a universal set of quantum gates in a 10-qubit quantum spin register.

Data Availability: The data that support the findings of this study are available from the authors upon request.

Competing Interests: The authors declare that there are no competing interests.

Author Information: Correspondence and requests for materials should be addressed to L.M.D. (lmduan@tsinghua.edu.cn).

Author Contributions: L.M.D. proposed the experiment and supervised the project. P.Y.H, F.W., X.Z.H., W.G.Z., X.L.O., X.W., X.-Y. Chang carried out the experiment. L.H. and W.Q.L. prepared the diamond sample. P.Y.H., L.H. and F.W. contribute equally to this experiment. P.Y.H, L.M.D., F.W. wrote the manuscript.

References

[1] Monz T, Schindler P, Barreiro J T, Chwalla M, Nigg D, Coish W A, Harlander M, Hansel W, Hennrich M and Blatt R 2011 *Phys. Rev. Lett.* **106** 130506
[2] Friis N, Marty O, Maier C, Hempel C, Holzapfel M, Jurcevic P, Plenio M B, Huber M, Roos C, Blatt R 2018 *Phys. Rev. X* **8** 021012
[3] Zhang J, Pagano G, Hess P W, Kyprianidis A, Becker P, Kaplan H, Gorshkov A V, Gong Z X and Monroe C 2017 *Nature* **551** 601
[4] Reiserer A, Kalb N, Blok M S, K J van Bemmelen, Taminiau T H, Hanson R, Twitchen D J and Markham M 2016 *Phys. Rev. X* **6** 021040
[5] Humphreys P C, Kalb N, Morits J P, Schouten R N, Vermeulen R F, Twitchen D J, Markham M and Hanson R 2018 *Nature* **558** 268
[6] Childress L and Hanson R 2013 *MRS Bull.* **38** 134
[7] Dutt M G, Childress L, Jiang L, Togan E, Maze J, Jelezko F, Zibrov A, Hemmer P and Lukin M 2007 *Science* **316** 1312
[8] Pfaff W, Hensen B, Bernien H, S B Van Dam, Blok M S, Taminiau T H, Tiggelman M J, Schouten R N, Markham M, Twitchen D J 2014 *Science* **345** 532
[9] S B Van Dam, Humphreys P C, Rozpkedek F, Wehner S and Hanson R 2017 *Quantum Sci. Technol.* **2** 034002
[10] Abobeih M H, Cramer J, Bakker M A, Kalb N, Markham M, Twitchen D and Taminiau T H 2018 *Nat. Commun.* **9** 2552
[11] Taminiau T H, Wagenaar J J T, T van der Sar, Jelezko F,

Dobrovitski V V and Hanson R 2012 *Phys. Rev. Lett.* **109** 137602
[12] Taminiau T H, Cramer J, T van der Sar, Dobrovitski V V and Hanson R 2014 *Nat. Nanotechnol.* **9** 171
[13] Goldman M L, Sipahigil A, Doherty M W, Yao N Y, Bennett S D, Markham M, Twitchen D J, Manson N B, Kubanek A and Lukin M D 2015 *Phys. Rev. Lett.* **114** 145502
[14] Casanova J, Wang Z Y and Plenio M B 2017 *Phys. Rev. A* **96** 032314
[15] Bernien H, Schwartz S, Keesling A, Levine H, Omran A, Pichler H, Choi S, Zibrov A S, Endres M, Greiner M 2017 *Nature* **551** 579
[16] Kelly J, Barends R, Fowler A G, Megrant A, Jeffrey E, White T C, Sank D, Mutus J Y, Campbell B, Chen Y 2015 *Nature* **519** 66
[17] *Ibm makes quantum computing available on ibm cloud*
[18] Song C, Xu K, Li H, Zhang Y R, Zhang X, Liu W, Guo Q, Wang Z, Ren W, Hao J 2019 *Science* **365** 574
[19] Yan Z, Zhang Y R, Gong M, Wu Y, Zheng Y, Li S, Wang C, Liang F, Lin J, Xu Y 2019 *Science* **364** 753
[20] Cramer J, Kalb N, Rol M A, Hensen B, Blok M S, Markham M, Twitchen D J, Hanson R and Taminiau T H 2016 *Nat. Commun.* **7** 11526
[21] Maletinsky P, Hong S, Grinolds M S, Hausmann B, Lukin M D, Walsworth R L, Loncar M and Yacoby A 2012 *Nat. Nanotechnol.* **7** 320
[22] Schirhagl R, Chang K, Loretz M and Degen C L 2014 *Annu. Rev. Phys. Chem.* **65** 83
[23] Lovchinsky I, Sushkov A O, Urbach E, N P de Leon, Choi S, K De Greve, Evans R, Gertner R, Bersin E, Muller C 2016 *Science* **351** 836
[24] Boss J M, Cujia K S, Zopes J and Degen C L 2017 *Science* **356** 837
[25] Schmitt S, Gefen T, Sturner F M, Unden T, Wolff G, Muller C, Scheuer J, Naydenov B, Markham M, Pezzagna S 2017 *Science* **356** 832
[26] Degen C L, Reinhard F and Cappellaro P 2017 *Rev. Mod. Phys.* **89** 035002
[27] Dolde F, Bergholm V, Wang Y, Jakobi I, Naydenov B, Pezzagna S, Meijer J, Jelezko F, Neumann P, Schulte-Herbrüggen T 2014 *Nat. Commun.* **5** 3371
[28] Arroyo-Camejo S, Lazariev A, Hell S W and Balasubramanian G 2014 *Nat. Commun.* **5** 4870
[29] G De Lange, Wang Z, Riste D, Dobrovitski V and Hanson R 2010 *Science* **330** 60
[30] Naydenov B, Dolde F, Hall L T, Shin C, Fedder H, Hollenberg L C L, Jelezko F and Wrachtrup J 2011 *Phys. Rev. B* **83** 081201
[31] Pham L M, Bar-Gill N, Belthangady C, D Le Sage, Cappellaro P, Lukin M D, Yacoby A and Walsworth R L 2012 *Phys. Rev. B* **86** 045214
[32] Liu G Q, Po H C, Du J, Liu R B and Pan X Y 2013 *Nat. Commun.* **4** 2254
[33] Bernien H, Hensen B, Pfaff W, Koolstra G, Blok M, Robledo L, Taminiau T, Markham M, Twitchen D, Childress L 2013 *Nature* **497** 86
[34] Kalb N, Reiserer A A, Humphreys P C, Bakermans J J, Kamerling S J, Nickerson N H, Benjamin S C, Twitchen D J, Markham M and Hanson R 2017 *Science* **356** 928
[35] Bonato C, Blok M S, Dinani H T, Berry D W, Markham M L, Twitchen D J and Hanson R 2016 *Nat. Nanotechnol.* **11** 247
[36] Cappellaro P 2012 *Phys. Rev. A* **85** 030301
[37] Griffiths R B and Niu C S 1996 *Phys. Rev. Lett.* **76** 3228
[38] Zu C, Wang W B, He L, Zhang W G, Dai C Y, Wang F and Duan L M 2014 *Nature* **514** 72
[39] Rong X, Geng J, Shi F, Liu Y, Xu K, Ma W, Kong F, Jiang Z, Wu Y and Du J 2015 *Nat. Commun.* **6** 8748
[40] Bradley C E, Randall J, Abobeih M H, Berrevoets R C, Degen M J, Bakker M A, Markham M, Twitchen D J and Taminiau T H 2019 *Phys. Rev. X* **9** 031045

Supplementary Material: Experimental Hamiltonian Learning of An 11-qubit Solid-State Quantum Spin Register

P.-Y. Hou*, L. He*, F. Wang*, X.-Z. Huang, W.-G. Zhang, X.-L. Ouyang, X. Wang, W.-Q. Lian, X.-Y. Chang, L.-M. Duan†[1]

[1] *Center for Quantum Information, Institute for Interdisciplinary Information Sciences, Tsinghua University, Beijing 100084, China*

PACS numbers: 03.67.-a

A. FREQUENCY MEASUREMENT BY THE ADAPTIVE QUANTUM PHASE ESTIMATION

An arbitrary frequency f can be written into a binary form $f = \sum_{i=1}^{N} 2^{i-1} \cdot k_i \cdot f_0 + \varepsilon$, where $k_i \in \{0, 1\}$ and $\varepsilon = \sum_{i=0}^{-\infty} 2^{i-1} \cdot k_i \cdot f_0$ is the uncertainty, $f_0 = \frac{1}{2^N t_{min}}$ as described in the main text. In the first Ramsey experiment with $t_1 = 2^{N-1} t_{min}$, the final phase $\phi_1 = 2\pi f t_1$ can be simplified as $\phi_1 = 2K\pi + k_1\pi + \alpha\pi$, where K is an unknown integer determined by $\{k_2, k_3, ..., k_N\}$ and $\alpha \in (0, 1)$ determined by ε. With $\vartheta_1 = \pi/2$, the probability

$$P_1 = \frac{1 + cos(\phi_1 - \vartheta_1)}{2} = \frac{1 + cos(k_1 + \alpha - 1/2)\pi)}{2}$$

If k_1=0, $P_1 = \frac{1+cos(\alpha-1/2)\pi}{2} > 0.5$; while if k_1=1, $P_1 = \frac{1+cos(\alpha+1/2)\pi}{2} < 0.5$. Hence, it gives us a way to estimate k_1. In the following Ramsey experiments, k_n can be estimated by the same way. While the phase produced by the already-measured digits $\{k_1, ..., k_{n-1}\}$ can be well determined and compensated by updating $\vartheta_{n+1} = \frac{\vartheta_n}{2} + \frac{k_n \pi}{2}$ to cancel out their influence to the probability P_n and reduce the fluctuation of the measurement outcomes.

B. SAMPLE AND EXPERIMENT SETUP

Sample description

The electronic grade diamond sample used in this work is produced by Element Six with a $\langle 100 \rangle$ crystal orientation and a natural abundance ($\sim 1.1\%$) of ^{13}C atoms. We fabricate a solid-immersion lens (SIL) on the surface at the site of a single NV center to enhance the fluorescence collection efficiency. The SIL fabrication procedure is following. We first search individual NV centers at the depth around $7 \sim 10$ μm under the surface, then obtain their precise coordinates (x, y, D) of each NV center according to the relative position to the references which are the pre-fabricated markers on the surface of the diamond sample, where D is the depth of a single NV center. Through numerical simulation, we calculate the optimal SIL radius as D/1.4 to achieve a minimized reflection for the NV fluorescence from the surface (Fig.1(a,b)). Subsequently, we apply a focused ion beam (FIB) with a hemisphere pattern (Fig.1.(d)) to fabricate SIL targeting on each NV center. For the NV center we use in this work, its fluorescence count rate ($\sim$750kHz) under 532nm laser illumination is enhanced about 7 times by the fabricated SIL.

After fabricating SILs for eight NV centers in Fig.1(c), we fabricate two 200nm-thickness gold striplines surrounding these SILs (black dots) to delivery the AC current. Each stripline are connected with two panels which are used to wire bonded with the microwave coplanar waveguide. Two gold electrodes which have a pointing difference of 120 degrees are fabricated for each SIL and used to adjust the local static electric field, although these electrodes are not used in this work.

Experiment Setup

We perform the experiment in a cryogenic temperature ($\sim$8K) high-vacuum ambient provided by a commercial cryostat (Nanoscale Workstation, Montana Instruments). Inside the cryostat, the sample is mounted on a 3-dimensional positioner from Attocube with sub-micrometer precision to address the SIL. We use a confocal microscopy, with an objective lens with NA =0.95 and a scanning galvo mirror (Thorlabs, GVS212), to address and detect single NV centers. Outside the cryostat, a permanent magnet is placed on the 3-axis motorized translation stage (PT3-Z8, Thorlabs) to provide an external magnetic field of 495 gauss for the NV centers. We align the magnetic field along

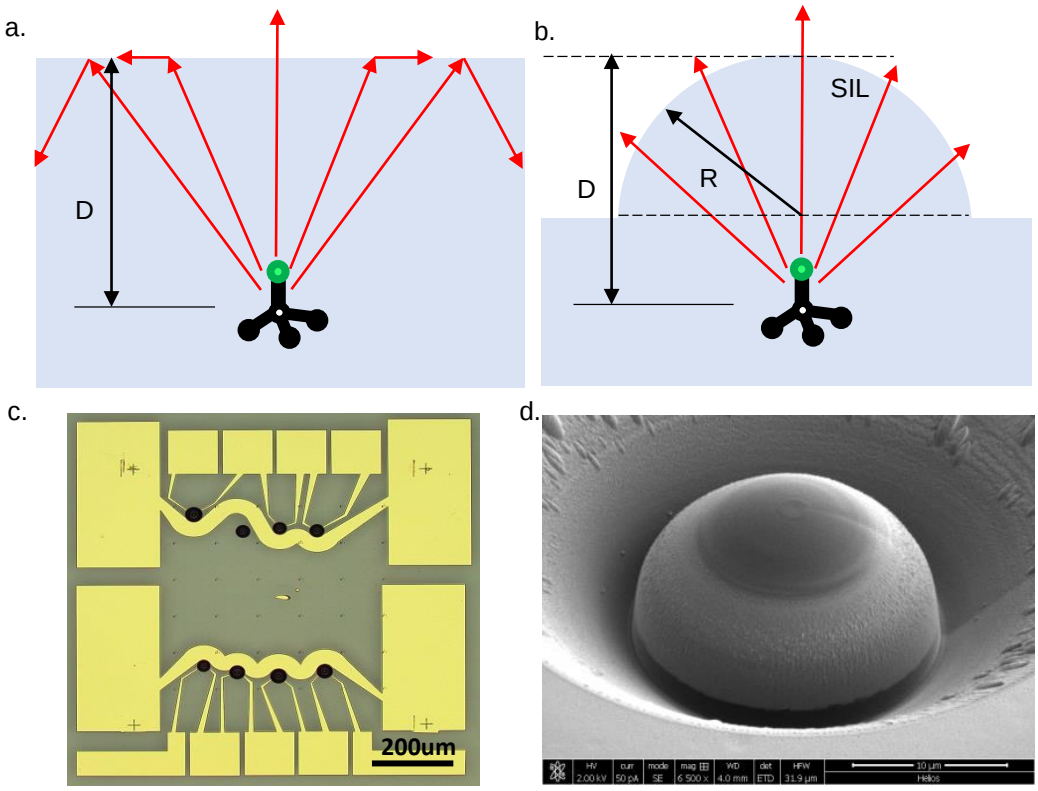

FIG. 1: **Solid-immersion lens.** (a,b) Sketch of fluorescence emission from a single NV center (a) without or (b) with a solid-immersion len. (c) Image of the sample surface under optical microscope. Each SIL (black circle) is surrounded by a stripline and two electrodes which are connected with two rectangular panels. Four crossings around the corners and black dot arrays are markers pre-fabricated on the surface. (d) Image of a SIL under scanning electron microscope.

the NV-symmetry axis by finding the position where $f = f_- + f_+$ is minimal ($\sim 2877.6MHz$ at 8K), where $f_\pm$ are the resonant frequencies of transitions $|0\rangle \leftrightarrow |\pm 1\rangle$. The readout and initialization of the electron spin are realized by two 637-nm continuous-wave lasers which are frequency-locked by a wavemeter (HighFinesse WS-7). A 532nm green laser is used to ionize the NV center to the negative charge state. We use three acoustic optical modulators (AOM) as optical switches to tailor these laser beams respectively.

Microwave field for coherently controlling NV electron spin is generated by using an IQ-mixer (Marki-microwave IQ-1545) to combine a microwave signal with $1.39GHz$ ($4.16GHz$) from a microwave source (Keysight N5181B) and two 100-MHz radio-frequency analog signals from an arbitrary-waveform generator (AWG, Tektronix 5014C). We modulate phase and amplitude of the RF signal by programming the AWG to tailor the experiment sequence with 1 ns time resolution. After IQ mixer, two amplifiers (Minicircuits ZHL-30W-252-S+ and a home-made amplifier) amplify two generated microwave signals with frequencies $1.49GHz$ and $4.26GHz$, respectively. We combine two microwave signals and subsequently delivery them to a coplanar waveguide (CPW) which is inside the cryostat and wire-bonded with the surface gold panels. The digital markers of AWG are used to switch the lasers and microwave signals and control the detection windows.

C. EXPERIMENT SCHEMATIC

By employing the technique introduced in Ref.[1, 2], we pre-check the charge state and resonance of the NV center with the readout and initialization lasers. We open two lasers together for a certain time and record the count of the NV fluorescence. We continue to run the following experiment only in the case that the count is beyond a threshold. After the pre-check, we initialize the nitrogen nuclear spin to state $|m_N = -1\rangle$ based on measurement[1]. In the case of success, we subsequently run the experiment sequences.

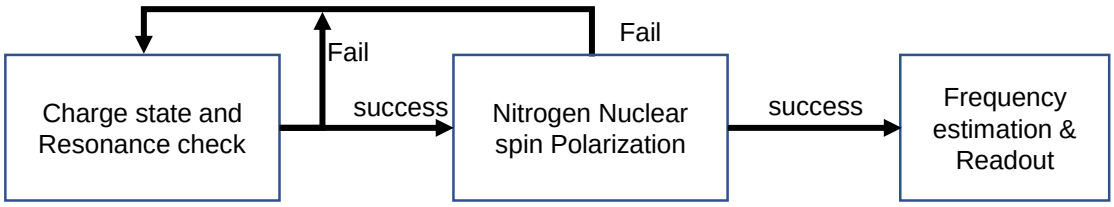

FIG. 2: **Experiment Schematic.**

D. HYPERFINE PARAMETER CALCULATION

Since the interactions between nuclear spins are negligible in our many-body system, we focus on Hamiltonian of the system composed of one NV electron spin and one nuclear spin. We consider a general form of Hamiltonian by taking into account the full hyperfine interaction tensor $\mathbf{A}$ as well as a random external magnetic field $\overrightarrow{B}$. We use Floquet theory to derive zeroth and first order approximation of the non-secular Hamiltonian, thus the full system Hamiltonian is diagonalized in the electron spin subspace.

Due to the C_s symmetry of the NV-^{13}C system, the hyperfine interaction takes the form: $H_{hfi} = A_{xx}S_xI_x + A_{yy}S_yI_y + A_{zz}S_zI_z + A_{zx}(S_xI_z + S_zI_x)$, where the Cartesian coordinate z is the NV principle axis, x lies in the plane expanded by the z axis and the target ^{13}C atom, $S_{x,y,z}(I_{x,y,z})$ are the spin operators for the electron and nuclear spin respectively. Furthermore, for weakly coupled ^{13}C nuclear spins, Fermi contact is ignored, thus we have the constraint $Tr(H_{hfi}) = A_{xx} + A_{yy} + A_{zz} = 0$. In an arbitrary external magnetic field, the system Hamiltonian can be described by

$$H = DS_z^2 + \omega_{ex}S_x + \omega_{ey}S_y + \omega_{ez}S_z + \omega_{nx}I_x + \omega_{ny}I_y + \omega_{nz}I_z + A_{xx}S_xI_x + A_{yy}S_yI_y + A_{zz}S_zI_z + A_{zx}(S_zI_x + S_xI_z) \quad (1)$$

where $\omega_{e(n)x(y,z)} = \gamma_{e(n)}B_{x(y,z)}$ and $B_{x,y,z}$ is the external magnetic field on the corresponding axis.

Afterwards, we go to the rotating frame of $U = e^{it(DS_z^2 + \omega_{ez}S_z)\otimes\mathbb{I}}$, the effective Hamiltonian becomes,

$$H_{eff} = H_0 + e^{i(D+\omega)t}H_{++} + e^{-i(D+\omega)t}H_{+-} + e^{i(D-\omega)t}H_{-+} + e^{-i(D-\omega)t}H_{--} \quad (2)$$

where

$$\begin{aligned}
H_0 &= A_{zz}S_zI_z + A_{zx}S_zI_x + \omega_{nx}I_x + \omega_{ny}I_y + \omega_{nz}I_z \\
H_{++} &= |+1\rangle\langle 0| \otimes \frac{1}{\sqrt{2}}(\omega_{ex}\mathbb{I} - i\omega_{ey}\mathbb{I} + A_{xx}I_x - iA_{yy}I_y + A_{zx}I_z) \\
H_{+-} &= |0\rangle\langle +1| \otimes \frac{1}{\sqrt{2}}(\omega_{ex}\mathbb{I} + i\omega_{ey}\mathbb{I} + A_{xx}I_x + iA_{yy}I_y + A_{zx}I_z) \\
H_{-+} &= |-1\rangle\langle 0| \otimes \frac{1}{\sqrt{2}}(\omega_{ex}\mathbb{I} + i\omega_{ey}\mathbb{I} + A_{xx}I_x + iA_{yy}I_y + A_{zx}I_z) \\
H_{--} &= |0\rangle\langle -1| \otimes \frac{1}{\sqrt{2}}(\omega_{ex}\mathbb{I} - i\omega_{ey}\mathbb{I} + A_{xx}I_x - iA_{yy}I_y + A_{zx}I_z)
\end{aligned} \quad (3)$$

Using the Floquet theory[3], the effective Hamiltonian can be highly approximated by the zeroth and first order approximation.

$$H_{eff} \approx H_{Floquet} = H_{eff}^0 + H_{eff}^1 \quad (4)$$

where $H_{eff}^0 = H_0$ and $H_{eff}^1 = \frac{1}{D+\omega_e}[H_{++}, H_{+-}] + \frac{1}{D-\omega_e}[H_{-+}, H_{--}]$.

This Hamiltonian after the Floquet approximation is diagonalized in the electron spin subspace, thus can be rewritten as

$$H_{Floquet} = |+1\rangle\langle +1| \otimes H_{n+} + |0\rangle\langle 0| \otimes H_{n0} + |-1\rangle\langle -1| \otimes H_{n-} \quad (5)$$

where

$$
\begin{aligned}
H_{n+} &= \begin{bmatrix} \frac{A_{zz}}{2} + \frac{\omega_{nz}}{2} + \frac{(A_{xx}-A_{yy})^2+(A_{zx}+2\omega_{ex})^2+4\omega_{ey}^2}{8(D+\omega_{ez})} & \frac{A_{zx}}{2} + \frac{\omega_{nx}-i\omega_{ny}}{2} + \frac{2A_{xx}\omega_{ex}+A_{yy}(A_{zx}-2i\omega_{ey})}{4(D+\omega_{ez})} \\ \frac{A_{zx}}{2} + \frac{\omega_{nx}+i\omega_{ny}}{2} + \frac{2A_{xx}\omega_{ex}+A_{yy}(A_{zx}+2i\omega_{ey})}{4(D+\omega_{ez})} & -\frac{A_{zz}}{2} - \frac{\omega_{nz}}{2} + \frac{(A_{xx}+A_{yy})^2+(A_{zx}-2\omega_{ex})^2+4\omega_{ey}^2}{8(D+\omega_{ez})} \end{bmatrix} \\
H_{n0} &= \begin{bmatrix} \frac{\omega_{nz}}{2} - \frac{D(A_{xx}^2+A_{yy}^2+(A_{zx}+2\omega_{ex})^2+4\omega_{ey}^2)-2A_{xx}A_{yy}\omega_{ez}}{4(D^2-\omega_e^2)} & \frac{\omega_{nx}-i\omega_{ny}}{2} - \frac{2DA_{xx}\omega_{ex}+A_{yy}(A_{zx}\omega_{ez}-2iD\omega_{ey})}{2(D^2-\omega_e^2)} \\ \frac{\omega_{nx}+i\omega_{ny}}{2} - \frac{2DA_{xx}\omega_{ex}+A_{yy}(A_{zx}\omega_{ez}+2iD\omega_{ey})}{2(D^2-\omega_e^2)} & \frac{-\omega_{nz}}{2} - \frac{D(A_{xx}^2+A_{yy}^2+(A_{zx}-2\omega_{ex})^2+4\omega_{ey}^2)+2A_{xx}A_{yy}\omega_{ez}}{4(D^2-\omega_e^2)} \end{bmatrix} \\
H_{n-} &= \begin{bmatrix} -\frac{A_{zz}}{2} + \frac{\omega_{nz}}{2} + \frac{(A_{xx}+A_{yy})^2+(A_{zx}+2\omega_{ex})^2+4\omega_{ey}^2}{8(D-\omega_{ez})} & -\frac{A_{zx}}{2} + \frac{\omega_{nx}-i\omega_{ny}}{2} + \frac{2A_{xx}\omega_{ex}-A_{yy}(A_{zx}+2i\omega_{ey})}{4(D-\omega_{ez})} \\ -\frac{A_{zx}}{2} + \frac{\omega_{nx}+i\omega_{ny}}{2} + \frac{2A_{xx}\omega_{ex}-A_{yy}(A_{zx}-2i\omega_{ey})}{4(D-\omega_{ez})} & \frac{A_{zz}}{2} - \frac{\omega_{nz}}{2} + \frac{(A_{xx}-A_{yy})^2+(A_{zx}-2\omega_{ex})^2+4\omega_{ey}^2}{8(D-\omega_{ez})} \end{bmatrix}
\end{aligned} \tag{6}
$$

The nuclear precession axis and frequency are calculated by

$$
\begin{aligned}
\overrightarrow{n}_i &= (Tr(\sigma_x H_{ni}), Tr(\sigma_y H_{ni}), Tr(\sigma_z H_{ni})), i = +, 0, - \\
f_i &= ||n_i||, i = +, 0, -
\end{aligned} \tag{7}
$$

Therefore, we are able to get the nuclear precession frequency

$$
\begin{aligned}
f_+ &= \sqrt{(\omega_{nz} + A_{zz} - \frac{A_{xx}A_{yy}}{2(D+\omega_{ez})} + \frac{A_{zx}\omega_{ex}}{D+\omega_{ez}})^2 + (\omega_{nx} + A_{zx} + \frac{A_{zx}A_{yy}}{2(D+\omega_{ez})} + \frac{A_{xx}\omega_{ex}}{D+\omega_{ez}})^2 + (\omega_{ny} + \frac{A_{yy}\omega_{ey}}{D+\omega_{ez}})^2} \\
f_0 &= \sqrt{(\omega_{nz} + \frac{A_{xx}A_{yy}\omega_{ez}}{D^2-\omega_{ez}^2} - \frac{2DA_{zx}\omega_{ex}}{D^2-\omega_{ez}^2})^2 + (\omega_{nx} - \frac{A_{zx}A_{yy}\omega_{ez}}{D^2-\omega_{ez}^2} - \frac{2DA_{xx}\omega_{ex}}{D^2-\omega_{ez}^2})^2 + (\omega_{ny} - \frac{2DA_{yy}\omega_{ey}}{D^2-\omega_{ez}^2})^2} \\
f_- &= \sqrt{(-\omega_{nz} + A_{zz} - \frac{A_{xx}A_{yy}}{2(D-\omega_{ez})} - \frac{A_{zx}\omega_{ex}}{D-\omega_{ez}})^2 + (-\omega_{nx} + A_{zx} + \frac{A_{zx}A_{yy}}{2(D-\omega_{ez})} - \frac{A_{xx}\omega_{ex}}{D-\omega_{ez}})^2 + (\omega_{ny} + \frac{A_{yy}\omega_{ey}}{D-\omega_{ez}})^2}
\end{aligned} \tag{8}
$$

In our experiment, the magnetic field around 495 gauss is near perfectly aligned along z axis so that $B_z \gg B_x, B_y$. In practical, B_x, B_y can only be bounded by 2.5 gauss, so that ω_{ex}, ω_{ey} are still in the level of several MHz which is much larger than the hyperfine strength of weakly coupled nuclear spins. We also have $D, \omega_{ez} \gg \omega_{ex}, \omega_{ey}$ due to the magnetic field orientation.

For example of f_+, we can neglect the third term in the first parenthesis, the second and third term in the second parenthesis and the entire third parenthesis, then perform zeroth and first order approximation to derive

$$
\begin{aligned}
f_+ &\approx \sqrt{(\omega_{nz} + A_{zz} + \frac{A_{zx}\omega_{ex}}{D+\omega_{ez}})^2 + (\omega_{nx} + A_{zx})^2} \\
&\approx f_{+,0} + \frac{(A_{zz}+\omega_n)A_{zx}\omega_{ex}}{f_{+,0}(D+\omega_e)} + \frac{A_{zx}\omega_{nx}}{f_{+,0}}
\end{aligned} \tag{9}
$$

where $f_{+,0} = \sqrt{(\omega_{nz} + A_{zz})^2 + A_{zx}^2}$. So we derive the deviation of f_+ as

$$
\Delta f_+ = f_{+,0} - f_+ \approx \frac{(A_{zz}+\omega_n)A_{zx}\omega_{ex}}{f_+(D+\omega_e)} + \frac{A_{zx}\omega_{nx}}{f_+} \tag{10}
$$

Analogously, we derive

$$
\Delta f_- = \frac{(A_{zz}-\omega_n)A_{zx}\omega_{ex}}{f_-(D-\omega_e)} - \frac{A_{zx}\omega_{nx}}{f_-} \tag{11}
$$

E. EXPERIMENT RESULTS

No.	$f_-/2\pi$ (kHz)	$f_+/2\pi$ (kHz)	$\omega_n/2\pi$(kHz)
1	1115.49(8)	-213.09(8)	530.177(4)
2	580.79(4)	489.77(4)	530.672(4)
3	520.25(8)	550.35(8)	530.657(4)
4	652.50(4)	418.36(4)	530.636(4)
5	537.61(4)	526.70(4)	530.615(5)
6	481.83(4)	581.02(4)	530.597(5)
7	577.74(4)	485.27(4)	530.578(5)
8	558.47(4)	504.42(4)	530.655(5)
9	559.88(4)	502.59(4)	530.569(5)
10	516.51(4)	545.08(4)	530.573(4)

TABLE I: **Frequency measurement result.** $f_\pm$ is measured by adaptive Ramsey-interferometry experiment. ω_n is estimated by using ODMR technique to measure the transition frequency $|0\rangle \leftrightarrow |\pm 1\rangle$.

No.	1	2	3	4	5	6	7	8	9	10
$N_{CX_{\pi/2}}$	10	38	14	30	26	56	56	34	52	65
$\tau_{CX_{\pi/2}}$	290	7649	20469	5487	30449	7401	28438	29824	11476	18638
$N_{X_{\pi/2}}$	23	25	62	24	90	122	58	95	81	261
$\tau_{CX_{\pi/2}}$	3632	3592	5704	1678	3664	7484	3598	3658	1964	3811
$N_{Z_{\pi/2}}$	4	4	4	4	4	4	4	4	4	4
$\tau_{Z_{\pi/2}}$	23	41	44	38	44	47	41	42	42	45
$N_{Z_{\pi/8}}$	1	1	1	1	1	1	1	1	1	1
$\tau_{Z_{\pi/8}}$	23	41	44	38	44	47	41	42	42	45

TABLE II: **Nuclear spin gate parameters**: π-pulse number N and interpulse delay time τ (ns). The magnetic field was calibrated before characterizing the nuclear spin gates.

F. GATE FIDELITY ESTIMATION

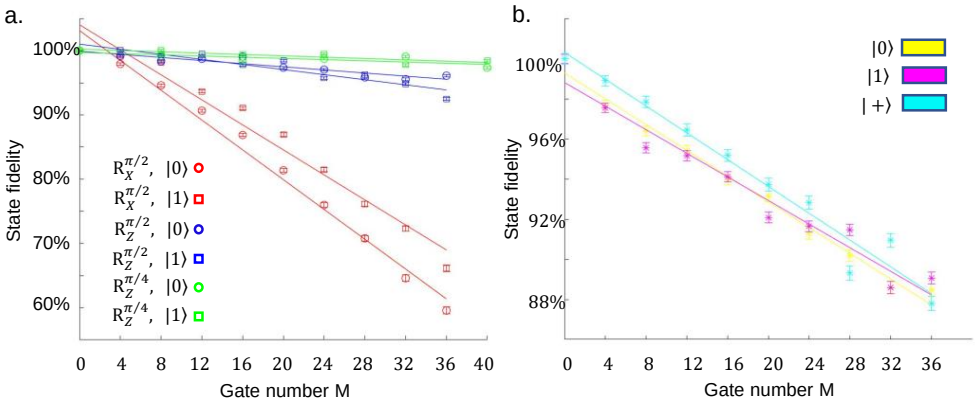

FIG. 3: **Gate fidelity estimation.** (a) State fidelity of the target nuclear spin decay as a function of the number of applied single-qubit gates with the initial electron spin state $|0\rangle$ and $|1\rangle$. (b) Fidelity of the joint electron-nuclear spin state decay curve with the initial electron spin state $|0\rangle$, $|1\rangle$ and $|+\rangle$. By fitting state fidelity decay curve with linear function, the slope is taken as gate infidelity.

To estimate gate fidelity, we prepare target nuclear spin in $|\uparrow\rangle$ and electron spin in $|0\rangle$ and $|1\rangle$ for single-qubit gates (additional $|+\rangle$ for two-qubit gate). Then we apply the same gate multiple times to make the net operation as an identity depending on the rotation angle. The maximal gate number varies with different gate and nuclear spin because AWG memory limits the total experiment sequence length $l < 32ms$. The lengths of gate sequences range from tens of nanoseconds to several milliseconds. Finally, we measure target nuclear spin state fidelity (joint electron-nuclear spin state fidelity) to ideal final state for single-qubit gates (two-qubit gate). To measure the joint electron-nuclear spin state fidelity to ideal state $|0\uparrow\rangle$, we perform ZI, IZ and ZZ measurements to derive the fidelity by the formula $F = (\langle ZI\rangle + \langle IZ\rangle + \langle ZZ\rangle + 1)/4$.

[1] L. Robledo Esparza, L. Childress, H. Bernien, B. Hensen, P. Alkemade, and R. Hanson, Nature: international weekly journal of science **477** (2011), ISSN 0028-0836.
[2] J. Cramer, N. Kalb, M. A. Rol, B. Hensen, M. S. Blok, M. Markham, D. J. Twitchen, R. Hanson, and T. H. Taminiau, Nature communications **7**, 11526 (2016).
[3] M. Leskes, P. Madhu, and S. Vega, Progress in nuclear magnetic resonance spectroscopy **57**, 345 (2010).